Experimental and numerical study of the effect of model geometric distortion on laboratory modelling of urban flooding

Xuefang Li[1*], Vasileios Kitsikoudis[2], Emmanuel Mignot[3], Pierre Archambeau[1], Michel Pirotton[1], Benjamin Dewals[1], Sébastien Erpicum[1]

[1] Hydraulics in Environmental and Civil Engineering (HECE), University of Liège (ULiège), Belgium

[2] Water Engineering and Management, Faculty of Engineering Technology, University of Twente, Enschede, The Netherlands

[3] LMFA, CNRS-Université de Lyon, INSA Lyon, Ecole Centrale de Lyon, Université Claude Bernard Lyon 1, France

[*]Corresponding author: Xuefang Li (xuefang.li@uliege.be)

Key points

- We evaluated the possible bias induced by geometric distortion in the case of laboratory scale modelling of urban flooding.
- In the tested configurations, this bias reached up to 17 % for the upscaled flow depths and 24 percentage points for the outlet discharge partition.
- For distortion ratios up to 5, this bias varies greatly, but it stabilizes asymptotically for larger distortion ratios.

Abstract

Laboratory studies of urban flooding often use geometrically distorted scale models due to the multi-scale nature of these specific flows. The possible bias induced by geometric distortion has never been thoroughly investigated with dedicated laboratory experiments. In this paper, we combine experimental and computational modelling to systematically assess the influence of the distortion ratio, i.e., the ratio of horizontal to vertical scale factors, on upscaled flow depths and discharge partition between streets. Three flow configurations were considered: a street junction, a street bifurcation and a small synthetic urban district. When the distortion ratio is varied up to a value of about 5, the upscaled flow depths at the model inlets decrease monotonously and the flow discharge in the branch that conveys the largest portion of the flow is greatly enhanced. For equal flow depths at the model outlets and depending on the configuration, the distortion effect induces a variation of the upstream flow depth approximately from ~4 % to ~17 % and a change in outlet discharge partition up to 24 percentage points. For a distortion ratio above 5, both upscaled upstream flow depths and outlet discharge partition tend to stabilize asymptotically. Our study indicates the direction and magnitude of the bias induced by geometric distortion for a broad range of flow cases, which is valuable for offsetting these effects in practical laboratory studies of urban flooding.

Keywords: experimental hydraulics; model scaling; urban flooding; distortion effect, numerical modelling

Plain Language Summary

Experimental data from laboratory scale models are a valuable complement to field data for validating computational models used for flood risk management. Geometrically distorted models (i.e., different horizontal and vertical scale factors) are widely used to downscale urban flooding in a network of streets. The possible biases induced by this geometric distortion have not been investigated extensively for this type of flows. This study combines experimental and computational modelling to systematically quantify the bias induced by geometric distortion in laboratory experiments simulating urban flooding.

1 Introduction

Flooding is a natural hazard with dire economic consequences that can even threaten human lives in extreme cases (Jonkman, 2005). The impact of flooding can become extremely severe particularly in densely populated urban areas. Consequently, the accurate estimation of urban flooding has become an integral component of flood risk management and assessment in times of climate change (Jenkins et al., 2017; Hettiarachchi et al., 2018; Liu et al., 2018) and rapid urbanization (Chen et al., 2015), while it is also needed to support adaptation strategies (Zhou et al., 2018).

Urban flooding is a complicated phenomenon due to intricate urban layouts, with flows in various branches meeting in junctions (Riviere et al., 2011; Schindfessel et al., 2015) or being divided in bifurcations (El Kadi Abderrezzak et al., 2011; Momplot et al., 2017). Hence, urban flooding needs to be modelled at least as 2D shallow flow (Mignot et al., 2006; Arrault et al., 2016) without any further simplifications, such as those that can be done in, for example, river flooding in more rural areas (Kitsikoudis et al., 2020).

Despite recent advances in numerical models, the accurate modelling of urban flooding and the estimation of flood hazard are hampered by a lack of reliable and detailed field data for proper validation of the numerical models (Rubinato et al., 2017; Teng et al., 2017; Wang et al., 2018; Costabile et al., 2020). Elevation data from remote sensing (Yu and Lane, 2006; Neal et al., 2009) can be very detailed but they show limitations as they can be obscured by surrounding buildings and other obstacles. Moreover, flood hazard mapping requires not only the inundation extent and the flow depth but also the flow velocities (Xia et al., 2014; Costabile et al., 2020; Musolino et al., 2020), which are very hard and potentially dangerous to obtain in flood conditions. As a result, only few studies have reported flow velocity data from measurements in urban floods. Brown and Chanson (2013) deployed an acoustic Doppler velocimeter in a street during the 2011 flood in Brisbane, Australia and highlighted the complexities of the post-processing of the field obtained turbulent flow velocity time-series. Perks et al. (2016) analysed the potential of unmanned aerial vehicles to provide data of surface flow velocity by monitoring features on the water surface and demonstrated their successful utilization in a flash flood in Alyth Burn, Scotland. Leitao et al. (2018) performed real-scale experiments in a laboratory facility to examine the potential of large-scale particle image velocimetry with the aid of surveillance camera footage and identified some critical points towards obtaining reliable data.

Recently there have been other alternatives that may offer data related to urban floods, such as footage from surveillance cameras in combination with machine learning (Vitry et al., 2019), data form citizen science (Assumpcao et al., 2018) and social media (Jongman, 2018), and reconstruction of past flood events with the aid of amateur photos and videos, news reports, etc. (Macchione et al., 2019). However, although such data from recent technological advances (McCabe et al., 2017) can undoubtedly be useful for flood risk assessment and management, their utilization for validation of numerical modelling is most of the time problematic because such datasets are usually incomplete and with uncertain boundary conditions. In addition, validation based on field data has only the ability to cover a range of events already observed; but not more extreme events for which model validation is also needed.

Physical modelling and experimental downscaling through similarity provide another option to establish benchmark datasets for numerical model validation (Rubinato et al., 2020). Urban flooding involves free surface flow, and downscaling from prototype scale (i.e. real-world) to model scale can be achieved with Froude similarity, i.e., by maintaining the ratio of inertia forces to gravity the same in the prototype and the physical model. Mignot et al. (2019) summarized the existing experimental studies related to urban flooding and noted that the horizontal scale factor, i.e., the ratio of a horizontal dimension in the prototype to the respective dimension in the physical model, varied from 30 to 200 in the literature. However, since urban flooding events are typically shallow flows in comparatively wide streets, if the horizontal and vertical scale factors are equal, the similarity between flows in the prototype and in the physical model will lead to extremely small flow depths in the laboratory that are hard to measure, and low flow velocities which tend to induce scale effects (Heller, 2011).

A way to overcome the problem of extremely small flow depths in the laboratory, and to attain a flow regime close to that of the prototype, is the utilization of geometrically distorted physical models. Such physical models have different horizontal and vertical scale factors (Kobus, 1984; Arndt et al., 2000), with the former typically being larger than the latter in the context of shallow flow. Geometrically distorted models have been successfully applied in river hydraulics, with some representative examples being the physical model of the Mississippi River (Chanson, 1999) with horizontal and vertical scale factors equal to 2000 and 100, respectively, and the physical model of Dargle River in Ireland (Novak et al., 2018) with horizontal and vertical scale factors equal to 100 and 50, respectively. There are some general guidelines for the preferable geometric distortion ratios in river modelling, such as Chanson (1999) suggesting it should not exceed 10. Very few studies discussed the influence of the selected geometric distortion on results of laboratory models; but they focused on other types of applications than urban flooding, such as hydraulic structures (Proudovsky, 1984; Wakhlu, 1984; Heller, 2011) or coastal engineering (Sharp and Khader, 1984). The effect of geometric distortion on physical models of urban flooding have not been investigated systematically based on dedicated experiments.

Smith et al. (2016) constructed a physical model of a floodway in Merewether, Newcastle, Australia with horizontal and vertical scale factors equal to 30 and 9, respectively, and validated the model with historical flood data. Güney et al. (2014) created a physical model of the town of Urkmez in Turkey with horizontal and vertical scale factors equal to 150 and 30, respectively, and investigated the collapse of the dam upstream of the town. Araud (2012) constructed a physical model of an idealized layout of an urban district with a large number of streets and intersections with a horizontal scale factor of 200 and a vertical scale factor of 20. The geometric distortion of an urban flooding model alters the flow aspect ratio, i.e., the ratio of flow depth to channel width, significantly (Li et al., 2019). This affects the losses and may introduce three-dimensional turbulent flow structures in the physical model that are not observed in prototype conditions. The geometric distortion effect on the upscaled flow depth and on the discharge partition in the intersections was investigated numerically by Li et al. (2020). This study showed that the distortion effect can introduce a bias of about 10 % when upscaling the data from the physical model to prototype conditions. However, this bias has not been studied with systematic experimental measurements nor has it been linked to the uncertainty that is introduced by experimental measurements.

Based on a combination of experimental observations and numerical modelling, the present study investigates the distortion effect in urban flood modelling using a physical model of a synthetic urban layout. Three different experimental setups are considered, with increasing complexity: a junction consisting of two inlets and one outlet, a bifurcation consisting of one inlet and two outlets, and a district model with three inlets, three outlets, and four intersections. The aim of this study is to: (i) quantify systematically the distortion effect on the upscaled flow depths at the inlets and on the discharge partition at the outlets, (ii) compare the results of a 2D shallow-water numerical model with experimental measurements, and (iii) analyse the effect of the measurements uncertainty on observed variables.

The paper is organized as follows: Section 2 presents the experimental setup, the studied cases, and the experimental and numerical methodology. Section 3 presents the experimental results for the upscaled flow depths at the inlets of the physical model and the discharge partition at the outlets, and Section 4 discusses the results. Finally, conclusions are drawn in Section 5.

2 Experimental setup and methodology

2.1 Experimental setup

The experiments were conducted in a physical model of a simplified urban district (Figure 1) at the Laboratory of Engineering Hydraulics at the University of Liege in Belgium. The model comprised a street network with four crossroads (Figure 2). Two of the crossroads had four branches and the other two had three branches, while all the intersections had an angle of 90°. The bottom side of the model was horizontal and made of smooth PVC with a roughness height equal to $k_s = 5\ 10^{-5}$ m, simulating the street surface. The street network was created by placing transparent Plexiglas sidewalls simulating the surrounding building blocks. The height of the sidewalls was 0.3 m and the width of each street in the model was constant and equal to $b_m = 0.2$ m. Assuming a horizontal scale factor, e_H, equal to 50, the model represents prototype-scale streets of $b_p = 10$ m in width (Li et al., 2020).

The flow in the physical model was steady and was recirculated in a closed system consisting of three inlets, three outlets, and a 2.4 m^3 bottom tank located underneath the physical model (Figure 2). All three inlets had the same incoming discharge, which was supplied at each inlet by a separate pump. The incoming discharges varied according to the examined case and were monitored with electromagnetic flowmeters (SIEMENS-MAG 5100W), with an accuracy of 0.5 %. At the entrance of each channel, right after the inlet, a baffle wall with a honeycomb pattern covering the whole cross-section was used to reduce the swirl and smoothen the incoming flow. The flow depth was regulated with adjustable weirs at the outlets that controlled downstream boundary conditions. The flow depths were measured at the inlets and the outlets with ultrasonic sensors (Microsonic: Mic+35/IU/TC), with an accuracy of ± 1 mm. The discharge through each of the three outlets was collected in separate straight and horizontal measurement channels, with a width of 0.2 m and a length of 1.5 m. A 90° triangular sharp-crested weir (Castex, 1969; Chanson and Wang, 2013) was placed at the downstream end of each channel (Figure 2c, Figure S1), which allowed the estimation of the flow discharge with calibrated rating curves based on the total head in the measurement channel. More details are provided in the supporting information (Text S1, Figures S1 and S2).

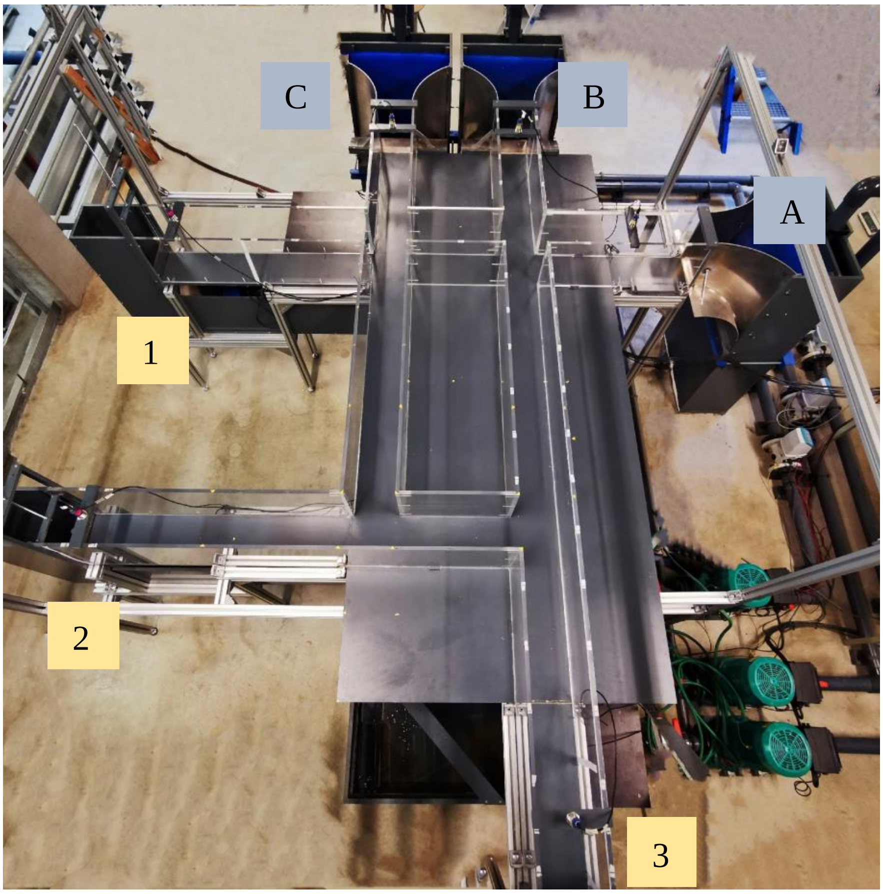

Figure 1. Physical model of the street network. The letters A – C and the numbers 1 – 3 denote the inlets and the outlets of the physical model, respectively.

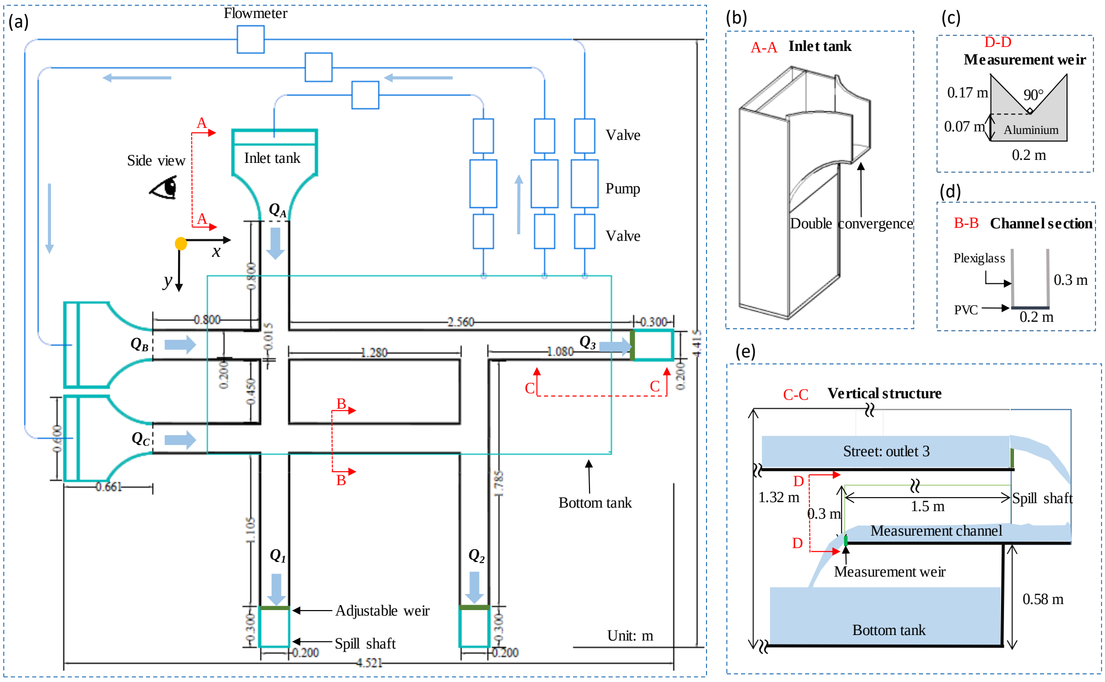

Figure 2. (a) Plan view and (b - e) details of the physical model of the street network.

2.2 Layouts of the experimental setup

To investigate systematically the distortion effect in the street network, we analysed three different geometric configurations with gradually increasing complexity by initially blocking the flow in some of the streets of the physical model. The three different cases were: (i) a junction model with two inlets and one outlet (Figure 3a); (ii) a bifurcation model with one inlet and two outlets (Figure 3b); (iii) a district model with all the inlets, outlets, and crossroads of the physical model (Figure 3c). In the junction and bifurcation models, the branches upstream of the single crossroad were 0.60 m long and the branches downstream were 1.28 m long. In the following, with notations N_{in} and N_{out} referring to the number of inlets and outlets, respectively: $N_{in} = 2$ and $N_{out} = 1$ in the junction case; $N_{in} = 1$ and $N_{out} = 2$ in the bifurcation case; $N_{in} = 3$ and $N_{out} = 3$ in the district case (Figure 3).

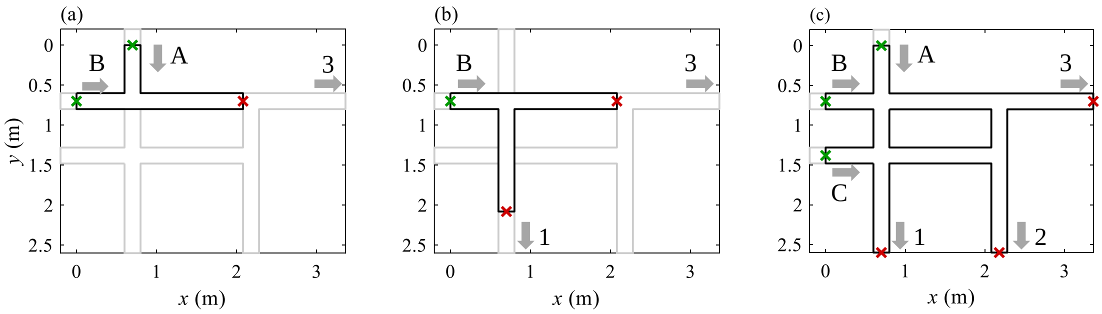

Figure 3. Layouts of the three experimental setups: (a) the junction model; (b) the bifurcation model; (c) the district model. Upstream and downstream flow depths were measured at the green and red crosses, respectively. The red crosses also define the locations where the downstream boundary condition was prescribed in the computations. Bold black lines sketch the domains used for the numerical modelling.

2.3 Measurement uncertainties

2.3.1 Flow depths

The measurements of the flow depth with the ultrasonic sensors are affected not only by the measurement uncertainty of ± 1 mm as mentioned in Section 2.1, but also by fluctuations of the water surface. These fluctuations were characterized by recording data with the ultrasonic sensor at a sampling frequency of 100 Hz for a time duration of minimum 60 s and estimating the mean and the standard deviation of the obtained time-series. For each test, the actual recording duration was adjusted (between 60 s and 150 s), to ensure stabilization of these statistics. The two types of uncertainties are indicated in the corresponding figures in Section 3.

2.3.2 Discharge partition

The uncertainties related to the discharge partition at the street outlets are associated with the measurement uncertainties of the flow discharges at the outlets of the physical model. A first source of uncertainty, although a small one, is the usage of rating curves based on the total head for the estimation of the outlet discharge. The induced relative error is of the order of 1 %, as the calibrated rating curves fit the experimental data well ($R^2 > 0.999$). The rating curves that were used in this study are presented in Figure S2 (in the supporting information).

A second source of uncertainty is related to the measurement of the flow depth, as described in the previous paragraph (i.e., uncertainties owed to the measurement accuracy of the ultrasonic sensor and the fluctuations of the water surface), and the way this affects the calculation of the total head for the estimation of the flow discharge at the outlets with the rating curves. In terms of mass balance, the differences between the measured total inflow and outflow discharges varied from 0.5 % to 2 % for the higher discharge range (≥ 3 m^3/h). When the outflow discharge was low (< 3 m^3/h), this uncertainty could lead to discharge measurement errors greater than 5 %. In such cases, manual measurements (volume filling rate) were also carried out to keep the mass balance errors below 2 %.

2.4 Numerical modelling

To complement the experimental observations, a series of numerical simulations were carried out for the three setups of Figure 3. The numerical modelling followed the same procedure as presented by Li et al. (2020). It consists in solving the 2D shallow-water equations on a Cartesian grid and by using a depth-averaged k-ε turbulence model for the estimation of eddy viscosity (Erpicum et al., 2009). The Darcy-Weisbach formulation with Colebrook-White equation was used for the estimation of bed shear stress, considering a roughness height for the bottom and side walls the same as in the laboratory model: $k_s = 5\ 10^{-5}$ m. The prescribed boundary conditions were the flow depth at the outlet of the branches and the discharge at the inlet of the branches. The mesh size used for all simulations was set to 0.005 m (i.e., 40 cells over the street width). A grid convergence analysis was presented by Li et al. (2020).

The computational tool was provided by the academic software Wolf (Erpicum et al., 2009). Although other modelling software could have been used, not all existing shallow-water solvers would have been successful in predicting the observed flow fields. Indeed, as demonstrated by Arrault et al. (2016). the turbulence closure implemented in the model is instrumental for capturing the correct shape, width and length of the recirculation zones downstream of each street intersection (see for instance Figure 10 in Arrault et al. (2016)). The academic model Wolf contains a suitable turbulence model (depth-averaged k-ε) to simulate most flow features of interest here (Arrault et al., 2016; Bruwier et al., 2017). Further details about the numerical model are provided by Li et al. (2020).

2.5 Flow configurations and examined cases

For a given layout of the laboratory setup (junction, bifurcation or district), an experimental run is defined by setting the value of the inflow discharge at the inlets (A, B, C in Figure 3) and of the flow depth at the outlets (1, 2, 3 in Figure 3). These parameters depend on one hand on the prototype-scale flooding scenario of interest and, on the other hand, on the considered horizontal and vertical scale factors, e_H and e_V, respectively. Therefore, like Li et al. (2020), we followed a two-step procedure to elaborate the test program and determine the model boundary conditions: (i) define prototype-scale flooding scenarios, and (ii) select scaling parameters. This procedure is summarized in a flow chart in Figure S3 (in the supporting information).

2.5.1 Prototype-scale flooding scenarios

Similarly to Li et al. (2020), we defined the prototype-scale flooding scenarios in quantitative terms by means of two parameters: a characteristic flow depth h_p representative of the flow depth at the downstream end of the streets, and a characteristic Froude number F.

Here, we assumed a prototype flow depth h_p equal to 0.5 m, which represents plausible urban flooding conditions. In all tests, the flow depths were considered the same at the different outlets of the street network, except for the bifurcation case, for which we additionally investigated cases with uneven flow depths at the outlets (Table 1). The difference between the outlets flow depths in the bifurcation case is expressed by the flow depth ratio, r, which is the ratio of the flow depth at the outlet 1 to the flow depth at the outlet 3 (Figure 3b). In this case, the flow depth in prototype conditions is considered equal to 0.5 m at the outlet 3. In the following, we note $h_{p,i}$ the prototype-scale flow depth at a specific outlet i (i = 1, 2, 3). For all tests, $h_{p,i}$ is simply equal to the characteristic flow depth h_p; except for outlet 1 in the bifurcation case where $h_{p,1} = r\, h_p$.

Then, a characteristic Froude number F was selected. By combining F with the prototype-scale flow depths $h_{p,i}$ at the outlets, characteristic values of the prototype outflow discharge $Q_{p,i}^{out}$ could be determined at the street outlets:

$$Q_{p,i}^{out} = \mathrm{F}\, b_p \sqrt{g}\; h_{p,i}^{\;3/2}, \tag{1}$$

where g is the gravitational acceleration. Note that $Q_{p,i}^{out}$ is not the actual outflow discharge at outlet i ($i = 1 \dots N_{out}$) in a specific run; but it is used for determining the inflow discharge according to Eq. (2). In all our tests, the inflow discharge was evenly distributed between the inlets (A and B in the junction case; A, B and C in the district case). Therefore, from a mass balance reasoning in steady state, the prototype-scale inflow discharge at the inlets was determined based on a pair of values for parameters h_p and F, as follows:

$$Q_p^{in} = \frac{1}{N_{in}} \sum_{i=1}^{N_{out}} Q_{p,i}^{out} = \frac{1}{N_{in}} \mathrm{F}\, b_p \sqrt{g} \sum_{i=1}^{N_{out}} \left(h_{p,i} \right)^{3/2} , \qquad (2)$$

where, Q_p^{in} is the inflow discharge at each inlet in prototype-scale.

To investigate the effect of flow velocity in the street network, several values of the characteristic Froude number F were tested. Its value ranges between 0.2 and 0.6, as detailed in Table 1.

2.5.2 Laboratory scaling

For free surface flows, similarity between the physical model and the prototype requires that the Froude numbers be equal in both configurations. To investigate the effect of geometric distortion on flow variables, we define the geometric distortion ratio, $d = e_H / e_V$, with $e_H = 50$ herein as mentioned in Section 2.1. In the experimental tests, the geometric distortion ratio d was varied by altering only the vertical scale factor e_V. The exact values of the considered scale factors in the experiments and in the computations are listed in Table S1 in the supporting information.

The range of distortion ratios applied in the experiments is narrower than in the numerical modelling (Table 1), due to limitations of the experimental setup. On one hand, laboratory tests with a distortion ratio $d = 1$ were not possible for the junction and the district models, due to too small inflow discharges (below 0.8 m^3/h) compared to the level of uncertainty of the flowmeters. On the other hand, the maximum values of distortion ratio d are generally smaller for the experiments than for numerical modelling, due to experimental limitations for the largest inflow discharges (i.e., limit of the pumps) or the highest flow depths (e.g., flow depth above 0.25 m, while the height of the street sidewalls is 0.3 m in the laboratory model). This highlights the valuable complementarity brought by the computations, which allow extending the ranges of tested parameters.

For a defined set of parameters h_p, F, e_H and d (or e_V), the flow depth $h_{m,i}$ to be prescribed at the outlet i of the physical model ($i = 1, 2, 3$) could be determined as: $h_{m,i} = h_{p,i} / e_V$ or $h_{m,i} = h_{p,i}\, d / e_H$ with $h_{p,i} = 0.5$ m (except for outlet 1 in the bifurcation model where it equals $r\, h_{p,}$). Similarly, the inlet discharge to be supplied at each inlet of the physical model is:

$$Q_m^{in} = \frac{1}{N_{in}} \mathrm{F}\, b_m \sqrt{g} \sum_{i=1}^{N_{out}} \left(h_{m,i}\right)^{3/2} = \frac{1}{N_{in}} \mathrm{F}\, b_p^{5/2} \sqrt{g} \sum_{i=1}^{N_{out}} \left(\frac{h_{p,i}}{b_p}\right)^{3/2} \frac{d^{3/2}}{e_H^{5/2}} \tag{3}$$

Equation (3) highlights that Q_m^{in} is entirely defined by an assumed prototype length scale (b_p), the studied case (N_{in} and N_{out}), the chosen values for F, e_H and d, as well as a non-dimensional flow depth in the prototype ($h_{p,i}$ / b_p).

Note that, since the Froude number F is introduced here for the sole purpose of defining the flooding scenarios, local values of the Froude number in the considered street networks considerably deviate from the value of parameter F. Local values of the Froude number typically exceed unity in the *vena contracta* downstream of the street intersections, as displayed in the maps of local Froude numbers computed by Li et al. (2020) (see their Figure 3).

2.5.3 Additional computations for uncertainty assessment

To analyse the combined effect of geometric distortion ratio and experimental uncertainties on the discharge partition in the bifurcation and district physical models, complementary numerical simulations were carried out by varying by 1 mm some of the outlet flow depths which serve as downstream boundary conditions. This sensitivity analysis was conducted as follows: (i) for the bifurcation model, we ran two additional numerical simulations for each d, by setting the outlet 1 flow depth 1 mm higher and lower than the nominal value; (ii) for the district model, we ran three additional numerical simulations for each d, by setting the flow depth 1 mm higher than the nominal value for each outlet at a time. These variations in boundary conditions are detailed in Table 1, together with a summary of all the investigated cases.

Table 1. Summary of experimental measurements and numerical simulations

			Experimental	Numerical	Boundary conditions	
Physical model	F (-)	r (-)	d_{exp} (-)	d_{num} (-)	Downstream	Upstream
Junction	0.4	1	[2 – 22.73]	[1 – 22.73]	$h_{m,3}$	$Q^{in}_{m,\mathrm{A}}$, $Q^{in}_{m,\mathrm{B}}$
	0.6	1	[2 – 17.54]	[1 – 25]		
Bifurcation	0.2	1	[1 – 17.54]	[1 – 17.54]		
	0.25	0.8	[1 – 16.67]	[1 -20]		
	0.3	0.7	[1 – 14.29]	[1 - 20]	$h_{m,1}$, $h_{m,3}$ $h_{m,1}$ – 1 mm, $h_{m,3}$ (1) $h_{m,1}$ + 1 mm, $h_{m,3}$ (1)	$Q^{in}_{m,\mathrm{B}}$ $Q^{in}_{m,\mathrm{B}}$ $Q^{in}_{m,\mathrm{B}}$
	0.3	0.8	[1 – 14.71]	[1 - 25]		
	0.3	1	[1 – 13.16]	[1 -20]		
	0.4	0.8	[1 – 12.5]	[1 - 25]		
District	0.2	1	[1.6 – 21.74]	[1 – 25]	$h_{m,1}$, $h_{m,2}$, $h_{m,3}$ $h_{m,1}$ + 1mm, $h_{m,2}$, $h_{m,3}$ (1)	$Q^{in}_{m,\mathrm{A}}$, $Q^{in}_{m,\mathrm{B}}$, $Q^{in}_{m,\mathrm{C}}$ $Q^{in}_{m,\mathrm{A}}$, $Q^{in}_{m,\mathrm{B}}$, $Q^{in}_{m,\mathrm{C}}$
	0.6	1	[1 – 13.7]	[1 - 25]	$h_{m,1}$, $h_{m,2}$ + 1mm, $h_{m,3}$ (1) $h_{m,1}$, $h_{m,2}$, $h_{m,3}$ + 1mm (1)	$Q^{in}_{m,\mathrm{A}}$, $Q^{in}_{m,\mathrm{B}}$, $Q^{in}_{m,\mathrm{C}}$ $Q^{in}_{m,\mathrm{A}}$, $Q^{in}_{m,\mathrm{B}}$, $Q^{in}_{m,\mathrm{C}}$

Notations: F is the characteristic Froude number; r the ratio of the prescribed flow depths at the outlets (details in Section 2.5.1); d_{exp}: the distortion ratios considered in the experiments; d_{num} the distortion ratios considered in the computations; $h_{m,1}$, $h_{m,2}$, $h_{m,3}$ the flow depths prescribed at the three street outlets (Figure 3); $Q^{in}_{m,\mathrm{A}}, Q^{in}_{m,\mathrm{B}}, Q^{in}_{m,\mathrm{C}}$ the discharges supplied at the three street inlets (Figure 3) as calculated from Eq. (3).

(1) For numerical computations only, not for the laboratory experiments.

3 Results

3.1 Distortion effect on flow variables for equal flow depth at the outlets

3.1.1 Flow depth at the inlets

To facilitate the comparisons between cases with different geometric distortion ratios, the flow depth measurements at the inlets and the corresponding numerical modelling results are converted to the prototype scale as a standardized prototype-scale flow depth, h^*, similar to Li et al. (2020), according to:

$$h^* = \frac{e_V h_{m,\mathrm{inlet}}}{e_H b_m} = \frac{h_{m,\mathrm{inlet}}}{d b_m} \quad (4)$$

When plotting h^* as a function of the geometric distortion ratio, it can be inferred that the uncertainty in the experimental results for the junction model (Figure 4a, 4b), the bifurcation model (Figure 4c, 4d), and the district model (Figure 4e, 4f), is greatest for low geometric distortion ratios ($d < 5$), as the corresponding vertical scale factors are large. This is owed mostly to the uncertainty induced by the ± 1 mm measurement accuracy of the ultrasonic sensor, which, as a percentage of the flow depth, becomes more prominent for small flow depths corresponding to low distortion ratios. Such measurement inaccuracies are amplified when the results are upscaled to prototype flow conditions (Eq. (4)). With the prototype flow depth $h_p = 0.5$ m and e_H being equal to 50, the flow depth in the physical model for $d < 5$ (i.e., $e_V > 10$) will be smaller than 5 cm. The uncertainty due to the measurement accuracy of the ultrasonic sensor gradually becomes smaller as the distortion ratio increases and the flow in the physical model gets deeper. The other source of uncertainty, the fluctuations in the water surface affecting the measurements of the flow depth, which is represented by the standard deviation of the time-series data, has a more erratic manifestation in the experimental data and appears to be independent of the distortion ratio.

There is a good agreement between experimental and numerical results of h^* for all cases (Figure 4) with the 2D shallow-water numerical model being able to reproduce the decreasing trend that the experimental measurements of h^* exhibit for increasing geometric distortion ratios. This decrease of h^* is steep for approximately $d < 5$, and the values of h^* almost stabilize for higher distortion ratio values. The observed decrease in h^* when d is increased may be attributed to a decrease in the relative roughness of the model material as the material remains unchanged when the geometric distortion is increased, as well as to an increase in the Reynolds number with the geometric distortion. Both effects tend to lower the frictional flow resistance.

The experimental standardized upscaled flow depth at the inlets, $h^*_{\exp}$, is for the most part slightly greater than the numerical standardized upscaled flow depth, h^*_{num}, for $d < 5$, particularly for the junction model (Figure 4a, 4b). The opposite trend is observed for $d > 10$, with this pattern being most notable for the district model (Figure 4e, 4f). This is further discussed in Section 4.2.

The distortion effect on the flow depth at each inlet, Δh^*, for the range of geometric distortion ratios that were tested, is quantified from:

$$\Delta h^* = \frac{h^*_{\max} - h^*_{\min}}{h^*_{\max}} \quad (5)$$

where h^*_{max} and h^*_{min} are respectively the maximum and minimum value of each curve in Figure 4.

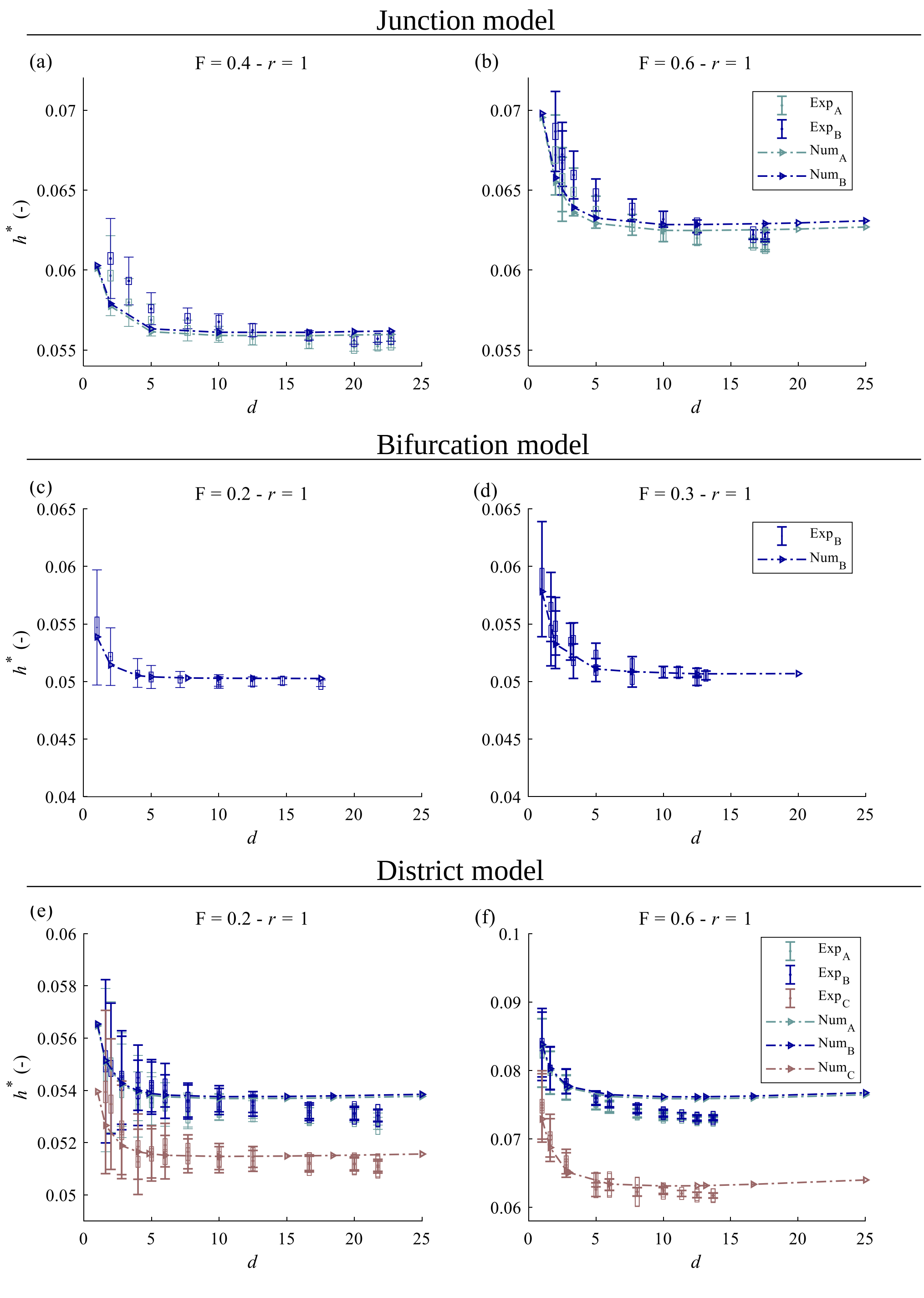

Figure 4. Standardized upscaled flow depth at the inlets h^* as a function of the geometric distortion ratio *d* for the junction model (Figure 3a) with (a) F = 0.4 and (b) F = 0.6; for the bifurcation model (Figure 3b) with (c) F = 0.2 and (d) F = 0.3; for the district model (Figure 3c), with (e) F = 0.2 and (f) F = 0.6. The uncertainty of the experimental measurements is expressed with boxplots, with the height of the boxes representing the standard deviation of the measurement time-series and the whiskers representing the 1 mm uncertainty associated with the instrumentation. The numerical results of the district model are the same as presented by Li et al. (2020).

Table 2 presents the experimental, Δh^*_{exp} , and numerical, Δh^*_{num}, results of Δh^*. The values of Δh^*_{exp} for the different cases vary from 4 % to 17 %, depending on the physical model and the flooding conditions. The flooding conditions are expressed by the Froude number F, the increase of which corresponds to an increase in Δh^* for all the inlets of every physical model (Figure 3). These results confirm that the choice of the distortion ratio in a scale model of flooding in an urban district may substantially affect the upscaled flow depths. The increase of Δh^* with the Froude number is more obvious in the bifurcation and district models than in the junction model, but this may be due to a difference in the ranges of considered distortion ratios (minimum value of 2 for the junction, while it is 1 in most other cases).

Table 2. Distortion effect on the standardized upscaled flow depths, Δh^*, at the inlets A, B, and C for all cases with r = 1 in Table 1.

Physical model	F (-)	d[1] (-)	Δh^*_{exp} (%)[2]			Δh^*_{num} (%)		
			A	B	C	A	B	C
Junction	0.4	[2 – 22.73]	7.81	8.03	-	6.9	6.79	-
	0.6	[2 – 17.54]	8.35	9.53	-	9.85	9.61	-
Bifurcation (r = 1)	0.2	[1 – 17.54]	-	8.96	-	-	6.71	-
	0.3	[1 – 13.16]	-	14.93	-	-	12.35	-
District	0.2	[1.6 – 21.74]	3.52	3.78	5.34	2.37	2.33	2.07
	0.6	[1 – 13.70]	12.02	13.05	16.92	9.22	9.10	13.33

(1) The range of tested distortion ratios is wider in numerical modelling than in the experiments, therefore, the distortion effect is quantified using the experimental range for both the numerical and experimental results to facilitate comparisons.
(2) More than one measurement was carried out for one distortion ratio in some tests. In these cases, the mean value of these measurements is used as h^* for the corresponding distortion ratio d to estimate the distortion effect.

3.1.2 Discharge partition

Discharge partition occurs in the bifurcation model with two outlets (Figure 3b) and in the district model with three outlets (Figure 3c). The numerical modelling results of discharge partition, $Q_{R,i}$, which is the percentage of the discharge at outlet i to the total outflow discharge, as a function of the geometric distortion ratio agree well with the experimental measurements for both the bifurcation (Figure 5a, 5b) and the district (Figure 5c, 5d) models.

In the bifurcation model, the single crossroad divides the upstream discharge into two branches: the discharge partition in the main branch, $Q_{R,3} = Q_3 / Q_B$, which is the extension of the branch with the incoming flow, and the discharge at the lateral branch, $Q_{R,1} = Q_1 / Q_B$, which is perpendicular to the main branch. $Q_{R,3}$ is always greater than $Q_{R,1}$. With an increase of geometric distortion ratio from 1 to 17.54 and from 1 to 13.16 for F = 0.2 and F = 0.3, respectively, the flow discharge in the main channel increases from around 70 % to 95 % of the total discharge (Figure 5a, 5b). This increase is steep for $d < 5$ and the discharge partitions in the main and the lateral channels tend asymptotically to a maximum and a minimum value, respectively, for distortion ratios higher than 5.

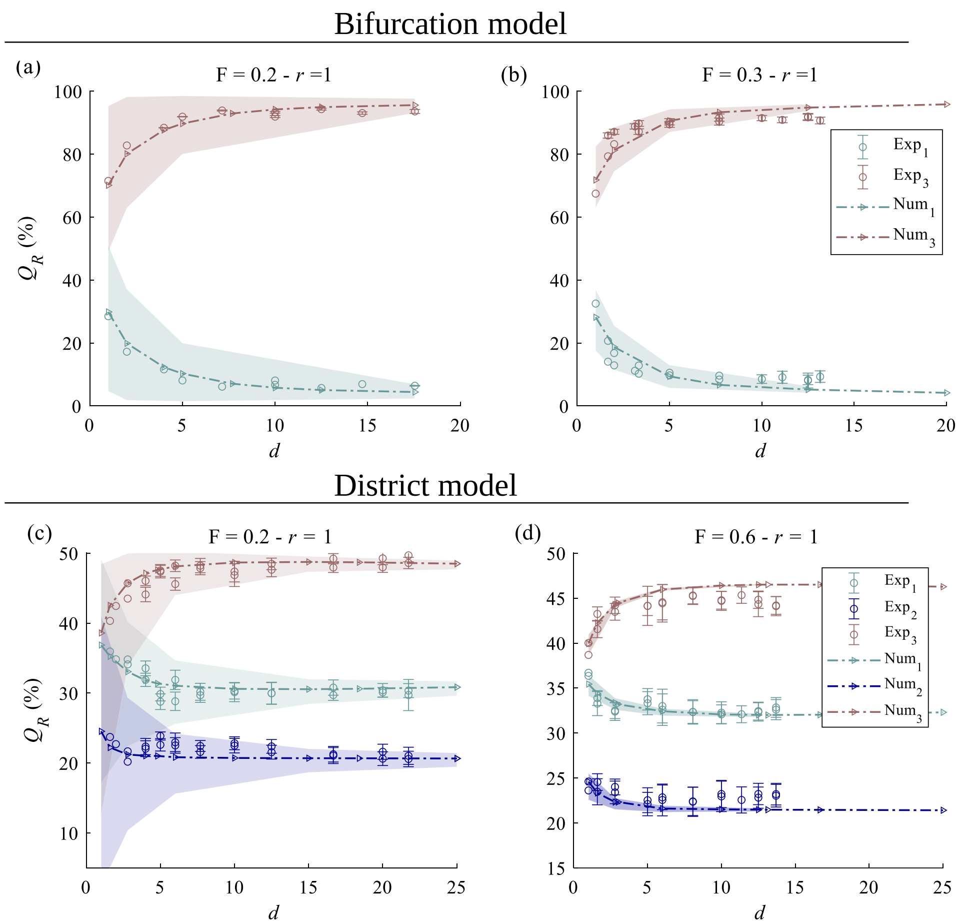

Figure 5. Discharge partition Q_R as a function of the geometric distortion ratio d for the bifurcation model (Figure 3b), with (a) F = 0.2 and (b) F = 0.3 and for the district model (Figure 3c), with (c) F = 0.2 and (d) F = 0.6. The whiskers represent the standard deviation of the time series of discharge partition. In case of the absence of whiskers, the outflow discharge was measured with 'volume filling' method as presented in Sect. 2.3.2. The shaded areas show the envelope of the computed results obtained by varying the flow depth at the outlet of the lateral branch by ± 1 mm, to assess the uncertainty associated with the accuracy of setting the downstream boundary condition in the

laboratory. The numerical results of the district model are the same as presented by Li et al. (2020).

While in general the numerical model reproduces the experimental measurements well, it slightly underpredicts the experimental discharges for $d < 5$ and overpredicts them for $d > 10$ for the main branch. The opposite trend is noted for the lateral branch. In the first case ($d < 5$), the computational results remain generally within the range of uncertainty of the experimental observations. For higher distortion ratios ($d > 10$), the flow depths become larger and three-dimensional flow structures are very likely to develop. This may be the reason why the computational model, based on the shallow-water equations, leads to some deviations compared to the observations, as further discussed in Section 4.2.

The district model exhibits a similar trend with the bifurcation model, with the discharge partition being altered at low geometric distortion ratios and getting stabilized after $d = 5$ (Figure 5c, 5d). Outlet 3 exhibits the greatest discharge for both tested F values and attains a slightly higher Q_R value, almost 50 %, for the lower F at high distortion ratios.

The distortion effect on the flow discharge partition, ΔQ_R, is quantified as the difference between the highest and lowest values of Q_R, $\Delta Q_R = Q_{R,\max} - Q_{R,\min}$, expressed in percentage points (pp). Table 3 shows that in the bifurcation model ΔQ_R from measurements is 22.7 pp and 24.4 pp, for F equal to 0.2 and 0.3, respectively, while it decreases significantly for the district model, where the maximum ΔQ_R value is found at outlet 3, which has the highest discharge, and is equal to 8.5 pp and 6.3 pp for F equal to 0.2 and 0.6, respectively. Contrary to the standardized upscaled flow depths at the inlets, where the distortion effect was greater for the higher values of F (Table 2), there is no notable pattern in the distortion effect on discharge partition with increasing F. This can be explained as follows: the upstream flow depths are representative of the cumulated effect of all losses across the considered flow domain. Therefore, they tend to increase with the flow velocity and the Froude number. In contrast, the discharge partition is controlled by the relative importance of losses occurring along the different possible flow paths. When the Froude number is increased, all losses certainly increase in absolute terms; but it is possible that their relative importance is not strongly affected by the change in the Froude number.

Therefore, the influence of varying the Froude number is considerably lower in the discharge partition than it is in the value of the flow depths at the inlets.

Overall, the analysis reveals that, depending on the model geometry, the discharge partition may be considerably affected by the model geometric distortion and this effect is generally well predicted by the 2D numerical model.

Table 3. Distortion effect on the discharge partition, ΔQ_R, at the outlets of the bifurcation and the district models.

Physical model	F (-)	$d^{(1)}$ (-)	$\Delta Q_{R,\mathrm{exp}}$ (pp)[(2)]			$\Delta Q_{R,\mathrm{num}}$ (pp)		
			1	2	3	1	2	3
Bifurcation	0.2	[1 - 17.54]	22.66	-	22.66	25.46	-	25.46
(r = 1)	0.3	[1 -13.16]	24.44	-	24.44	24.02	-	24.02
District	0.2	[1.6 – 21.74]	5.81	2.64	8.46	4.41	1.57	5.98
	0.6	[1 – 13.70]	4.37	1.92	6.3	3.34	3.12	6.56

(1) The range of tested distortion ratios is wider in numerical modelling than in the experiments, therefore, the distortion effect is quantified using the experimental range for both the numerical and experimental results to facilitate comparisons.

(2) More than one measurement was carried out for one distortion ratio in some tests. In these cases, the mean value of these measurements is used as Q_R for the corresponding distortion ratio d to estimate the distortion effect.

3.2 Distortion effect on flow variables for uneven flow depth at the outlets

In each test discussed in Section 3.1, the same flow depth was prescribed at the different street outlets. To broaden the scope of the study, this section examines how the distortion ratio affects the upstream flow depth and the discharge partition when the flow depths at the different outlets are not equal. To simplify the analysis, we present results only for the bifurcation model (Figure 3b). The tested cases for various r and F values are detailed in Table 1 and in Section 2.5.3.

Figure 6 shows that the values of h^* at the inlet of the bifurcation model decrease monotonously with increasing geometric distortion ratio for all cases, similar to the experiments where the flow depths at the outlets were the same (Figure 4c, 4d), which means that the variation of r from 0.7 to 1 and F from 0.25 to 0.4 does not affect this general trend. When the ratio r of downstream flow depths is varied from 0.7 to 1 while keeping F equal to 0.3, the effect of distortion remains similar (Table 4). On the contrary, the increase of F from 0.25 to 0.4 for r = 0.8 highly influences the distortion effect, which varies between 10 % and 25 % (Table 4). This agrees with the findings of

Section 3.1, where the distortion effect on flow depths becomes more prominent with increasing F (Table 2) for equal flow depths at the two outlets of the bifurcation model (r = 1).

Table 4. Distortion effects on the standardized upscaled flow depth, Δh^*, at the inlet and the discharge partition, ΔQ_R, at the outlets of the bifurcation model for various combinations of Froude number, F, and flow depth ratio, r.

	F	r	$d^{(1)}$	Δh^*_{exp} (2)	Δh^*_{num}	$\Delta Q_{R,\text{exp}}$ (2)	$\Delta Q_{R,\text{num}}$
	(-)	(-)	(-)	(%)	(%)	(pp)	(pp)
Bifurcation model	0.3	0.7	[1 - 14.29]	12.54	13.46	33.4	18.31
	0.3	0.8	[1 - 14.17]	19.36	16.23	6.23	2.08
	0.3	1	[1 – 13.16]	14.93	12.35	24.44	24.02
	0.25	0.8	[1 – 16.17]	9.61	11.68	31.74	13.98
	0.4	0.8	[1 – 12.50]	25.11	21.51	15.69	18.17

(1) The range of tested distortion ratios is wider in numerical modelling than in the experiments, therefore, the distortion effect is quantified using the experimental range for both the numerical and experimental results to facilitate comparisons.

(2) More than one measurement was carried out for one distortion ratio in some tests. In these cases, the mean value of these measurements is used for h^* and Q_R for the corresponding distortion ratio d.

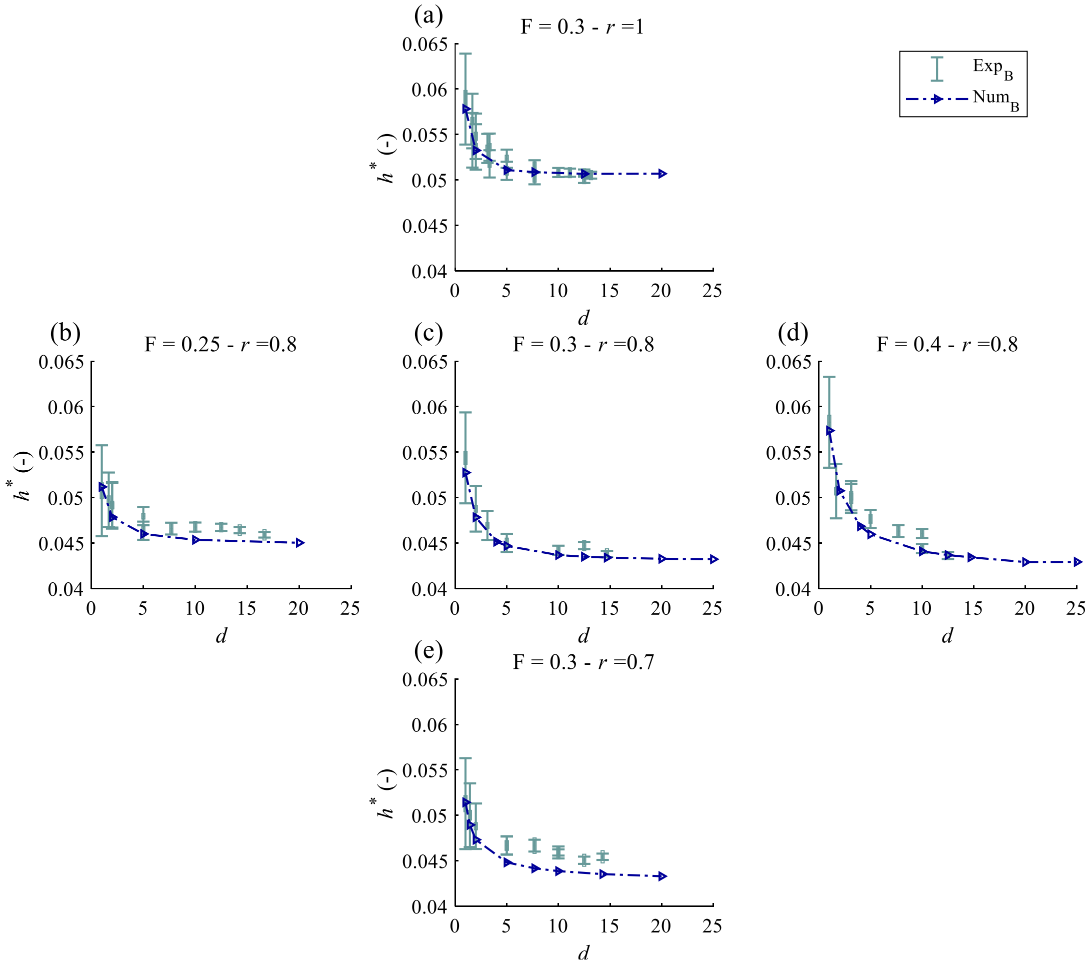

Figure 6. Standardized upscaled flow depth at the inlet B, h^*, as a function of the geometric distortion ratio, d, for the bifurcation model (Figure 3b) for various combinations of r and F. The figure layout is such that each row corresponds to a particular value of parameter r and each column corresponds to a particular value of the Froude number F. The uncertainty of the experimental measurements is expressed with boxplots, with the height of the boxes representing the standard deviation of the measurement time-series and the whiskers representing the 1 mm uncertainty associated with the instrumentation. Note that Figure 6a is same with Figure 4d.

The variation of the ratio r in the bifurcation model has a much greater impact on the discharge partition compared to the inlet flow depth. Figure 7 shows the discharge partition in the bifurcation model for the same variations of r and F as in Figure 6 for the flow depth. Contrary to h^*, which maintained qualitatively the same trend for every combination of r and F, the pattern of discharge partition gets radically altered. For $r = 1$ and F = 0.3, the largest portion of the flow is conveyed by the main channel ($Q_{R,3} > Q_{R,1}$, also in Figure 5). As r decreases to 0.7 (with F remaining equal to 0.3), the lateral branch gradually conveys the largest portion of the flow ($Q_{R,1} > Q_{R,3}$). The same pattern is also observed when F varies between 0.25 and 0.4 with $r = 0.8$. This is consistent with findings of Riviere et al. (2014), who showed that the portion of discharge reaching the lateral branch (outlet 1) decreases when the Froude number is increased (Figure 7b-d).

Nevertheless, qualitatively the influence of the distortion ratio on the discharge partition is similar for every case shown in Figure 7, with increasing values of d enhancing the flow discharge at the branch that carries the largest portion of the flow, with the exception of F = 0.3 and $r = 0.8$, for which the flow discharges at the two branches are almost equal (Figure 7). The ΔQ_R results are summarized in Table 4, which shows that the distortion effect on the observed discharge partition seems to vary non monotonously when r or F are varied.

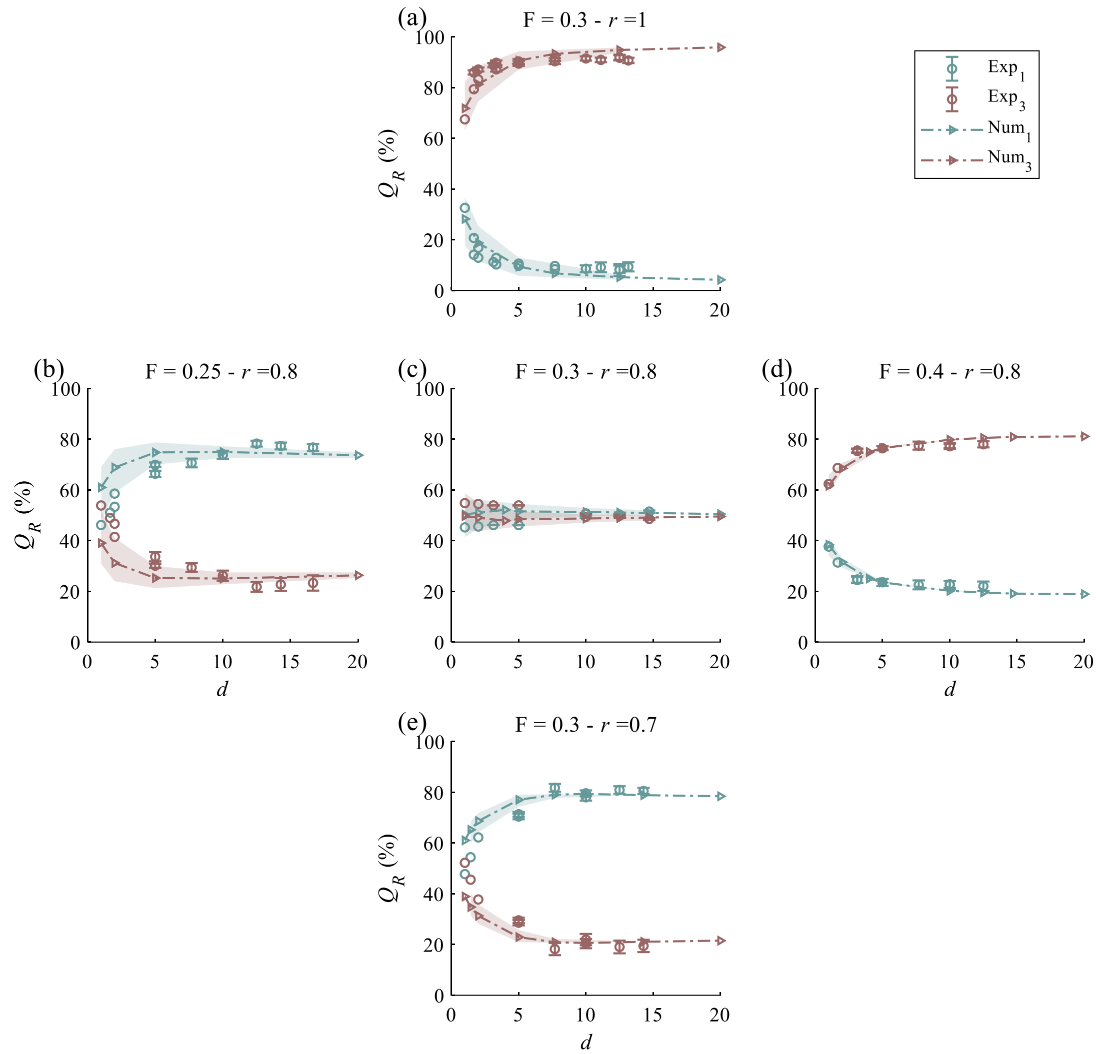

Figure 7. Discharge partition, Q_R, as a function of the geometric distortion ratio, d, for the bifurcation model (Figure 3b) for various combinations of r and F. The figure layout is such that each row corresponds to a particular value of parameter r and each column corresponds to a particular value of the Froude number F. The shaded areas show the extreme numerical results when varying the flow depth at the outlet 1 by ± 1 mm, to express the uncertainty associated with the experimental inaccuracies in setting the downstream boundary conditions. Note that Figure 7a is same with Figure 5b.

4 Discussion

4.1 Sensitivity analysis

To quantify the uncertainty associated with imperfect setting of the downstream flow depth in the experiments, we conducted a sensitivity analysis by varying some of the downstream flow depths by 1 mm (see Section 2.5.3 and Table 1) and simulating numerically the discharge partition for each case.

The results of this sensitivity analysis are presented as shaded areas in Figure 5. The vertical extension of these shaded areas for each d is defined by the maximum and minimum values obtained from the numerical modelling when varying the flow depth at the outlets by 1 mm. The larger the shaded area, the more sensitive the discharge partition to the variation of the downstream boundary condition and as a result, the larger the uncertainty potentially affecting the experimental observations.

There are two main findings regarding the uncertainty of the discharge partition: (i) the effect of the uncertainty from setting the downstream water depth becomes considerably smaller in all branches for all distortion ratios when the value of F increases; (ii) for a given value of F, the uncertainty decreases when the geometric distortion ratio increases, because this 1 mm, as a percentage of the flow depth, becomes less important for high flow depths corresponding to large distortion ratios. For example, the height of the shaded area in the bifurcation model for F = 0.2 is reduced approximately from 46 pp to 5 pp for increasing d (Figure 5a). For F = 0.3, this variation becomes significantly smaller and ranges approximately from 19 pp to 2 pp (Figure 5b). Similarly, in the district model for F = 0.2, the height of the shaded area of $Q_{R,3}$ decreases from 30 pp to 1 pp with increasing d, but for F = 0.6 the height of the shaded area becomes very small and varies from 2.5 pp to 0.3 pp. These results highlight that minor inaccuracies in setting the downstream boundary condition can largely affect the discharge partitions for the cases of low F and small distortion ratio (i.e., in case of small flow depths), while the discharge partition at highly distorted models is less influenced by measurement uncertainties.

As shown in Figure 7, uncertainty in setting the downstream flow depth affects the discharge partition in a similar way irrespective of the ratio r of downstream flow depths: this effect is considerably reduced when either the Froude number F or the distortion ratio d is increased.

4.2 Agreement between experimental observations and numerical modelling

Although there is an overall good agreement between the experimental measurements and the numerical simulations, there are some cases where the 2D numerical model systematically overpredicts or underpredicts the experimental data. In the junction and district cases, it is particularly the case for large values of F and large values of d, where the effect of the uncertainty from setting the downstream water depth is rather small. For instance, in the district model, the numerical model overpredicts h^* (Figure 4e, 4f) and the discharge in outlet 3 (Figure 5d), which is the largest discharge, for approximately $d > 10$. To quantify these discrepancies, we estimated the bias between experimental measurements and numerical modelling for the standardized upscaled flow depth $\Delta h^*_{\text{num-exp}}$, and the discharge partition $\Delta Q_{R,\text{num-exp}}$, respectively, from:

$$\Delta h^*_{\text{num-exp}} = \frac{h^*_{\text{num}} - h^*_{\text{exp}}}{h^*_{\text{exp}}} \tag{6}$$

$$\Delta Q_{R,\text{num-exp}} = Q_{R,\text{num}} - Q_{R,\text{exp}} \tag{7}$$

Figure 8 presents the results of Eqs. (6) and (7) as a function of the street aspect ratio, $h_{m,i} / b_m$, where $h_{m,i}$ is the flow depth at the outlet, for all cases with $r = 1$. Figure 8b focuses on the branch that carries the largest portion of the flow, which is outlet 3 both for the bifurcation and the district models. For the shallower flows with $h_{m,i} / b_m < 0.4$, the numerical model mostly underpredicts the measurements of h^* (Figure 8a), while it tends to underpredict Q_R in the bifurcation case and overpredict Q_R in the district case (Figure 8b). For $h_{m,i} / b_m > 0.4$, the numerical model systematically overpredicts both h^* and Q_R in the branch with the largest discharge, with differences up to 4 %.

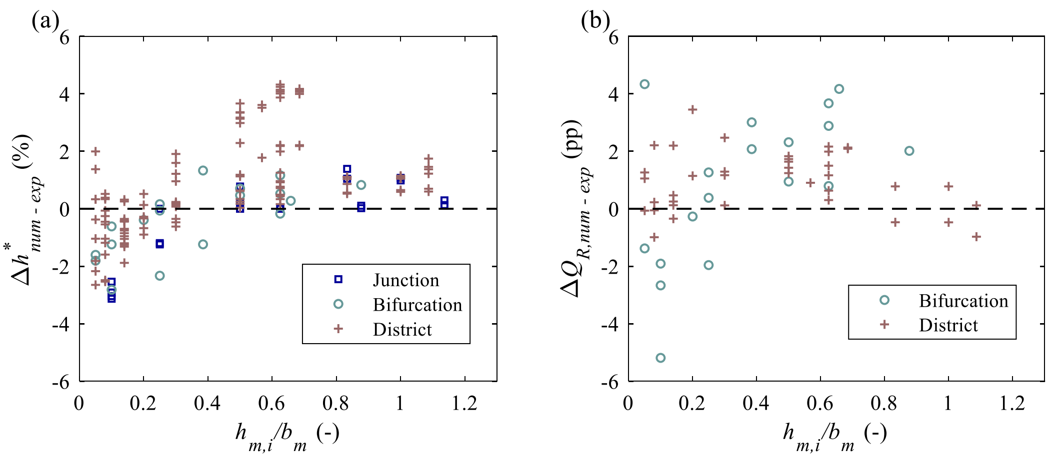

Figure 8. Differences between experimental measurements and numerical results for (a) the standardized upscaled flow depth at the inlet, $\Delta h^*_{\text{num-exp}}$, and (b) discharge partition, $\Delta Q_{R,\text{num-exp}}$, as a function of the street aspect ratio, $h_{m,i} / b_m$, near outlet 3. The $\Delta Q_{R,\text{num-exp}}$ results are from the branches that convey the largest portion of the flow, i.e., from outlet 3 in both the bifurcation model with $r = 1$ (Figure 3b) and the district model (Figure 3c).

Urban flooding in prototype conditions usually occurs as shallow flow, meaning that the vertical velocity component can be considered negligible. With increasing distortion ratio, the flow depth in the physical model also increases and the three-dimensional characteristics of the flow in the model tend to be augmented. While a Froude similarity between the physical model and the prototype is satisfied, a deep flow in the physical model with large geometric distortion ratio will be affected by three-dimensional flow structures (El Kadi Abderrezzak and Paquier, 2009). Such three-dimensional flow patterns do not necessarily occur in prototype conditions and cannot be captured by a 2D shallow-water numerical model, such as the one employed in this study. This could explain some discrepancies between experimental and numerical results for high geometric distortion ratios.

In their computations, Li et al. (2020) found a slight non-monotonous variation pattern of the values of h^* and the discharge partition with increasing geometric distortion ratio for the district model, with the flow variables firstly decreasing and then slightly increasing. This trend is detected in the experimental data of the discharge partition for high values of F in the district model (Figure 5d); however, the observed variation is of similar magnitude as the experimental uncertainty. This non-monotonous trend is not exhibited in the measurements of h^* (Figure 4e, 4f), which seem to decrease monotonously with increasing geometric distortion ratio. Li et al. (2020) hypothesized that the non-monotonicity in the computational results may be attributed to a competition between decreasing frictional losses and increasing local losses as the distortion ratio becomes larger. However, it is likely that the latter effect is not captured accurately by a 2D shallow-water model which does not resolve three-dimensional flow structures.

4.3 Implications for practice

4.3.1 Pros and cons of model geometric distortion

The design of a particular hydraulic scale model results generally from a trade-off between on one hand cost-efficiency and technical constraints (requiring a relatively large value for e_H) and on the other hand fulfilment of ideal hydraulic specifications (which usually advocate for the use of considerably smaller e_H values). This is particularly true for urban flooding, as well as other shallow flows developing over relatively large spatial extents. Determining the value of the vertical scale factor e_V (or equivalently of the distortion ratio $d = e_H / e_V$) remains also intricate. The benefit of opting for a relatively large value of d (i.e., relatively small value of e_V) is at least threefold:

1. a reduction of the relative uncertainties in the measurements, and hence in the estimation of the upscaled flow variables, as shown by the whiskers in Figure 4 and Figure 6;
2. a flow regime in the scale model closer to the fully turbulent regime encountered at prototype-scale, since the Reynolds number in the model increases with the power 3 / 2 of d;
3. thanks to a higher flow depth in the model, mitigation of surface tension effects, and excessive intrusion effects in case of probe measurements (e.g., ADV), among others.

These benefits are obtained at the expense of an excess of the depth-to-width aspect ratio of the flow in the model compared to the prototype. As highlighted by a power balance analysis conducted by Li et al. (2020), this excess of aspect ratio tends to reduce the rate of energy losses, and alters the relative importance of various dissipation mechanisms (e.g., horizontal vs. vertical shear stresses). These are the reasons why, depending on the geometric distortion selected by the modeller, the flow depths at the inlets vary by up to 15 % and the discharge partition by up to 25 pp in the configurations tested here (Figure 9). These variations are comparable to, or even exceed, other sources of uncertainties affecting urban flood modelling (e.g., design discharge, topographical details…, see Paquier et al. (2020)), and they are certainly not negligible from an engineering perspective.

Although present results show the sensitivity of the predicted flow variables to the geometric distortion, they do not give a clue on which value of d leads to the "correct" prediction at prototype scale. Indeed, a complete similarity of the real-world flow needs to consider the scaling of the frictional losses (in addition to present Froude similarity). This may require a careful selection of the model material, which will depend on the actual roughness height characterizing the prototype, hard to determine due to non-uniformity of roughness elements, micro-topography, and complex geometric features present in real-world urban areas.

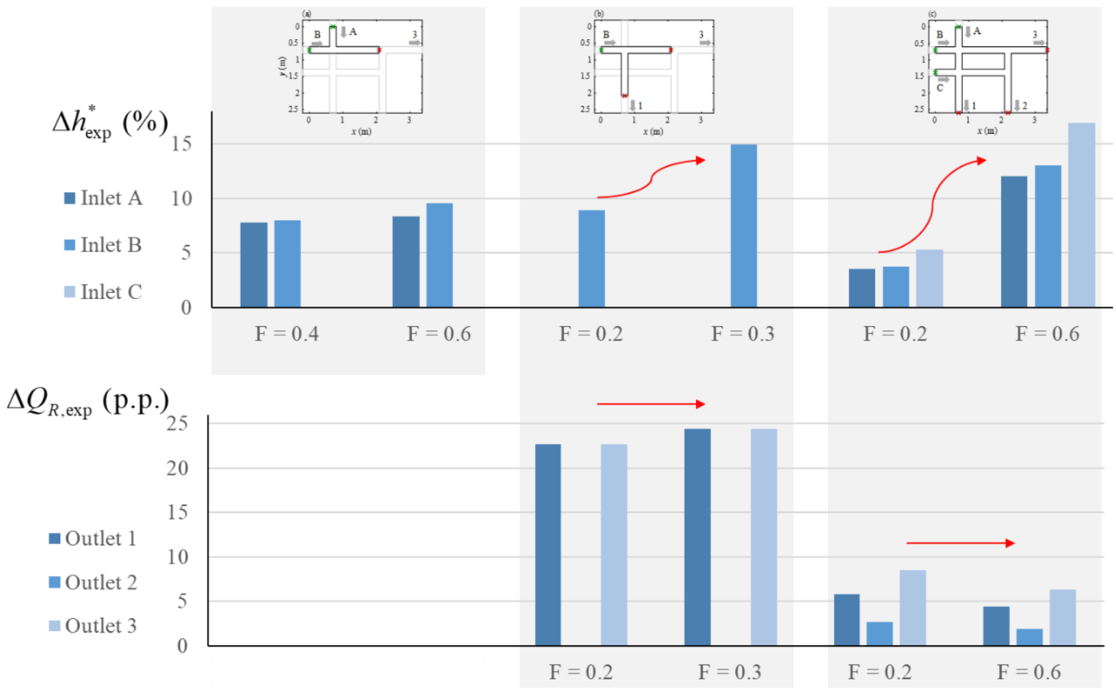

Figure 9. Summary of the influence of model geometric distortion on the flow depth at the inlets ($\Delta h^{*}_{\text{exp}}$) and on the discharge partition ($\Delta Q_{R,\text{exp}}$) for the three experimental urban layouts described in Figure 3 (junction, bifurcation and district) with an equal flow depths prescribed at the outlets (r = 1). The red arrows sketch the variation of $\Delta h^{*}_{\text{exp}}$ and $\Delta Q_{R,\text{exp}}$ with the Froude number F.

In theory, the bed friction number S should be kept the same in the model as at prototype scale, with S defined as $S = c_f L / (2 H)$ where c_f is the friction coefficient, L a characteristics horizontal length scale (e.g., the street width) and H a characteristic flow depth. However, keeping the bed friction number S_m in the model equal to that at the prototype S_p is hardly possible in practice for two reasons.

- First, the value of $k_{s,m}$ required to ensure $S_m = S_p$ changes with the considered flow scenario. Since a scale model is usually built to explore a range of flow scenarios, it would require tedious and costly changes of the model material for each considered flow scenario.
- Second, achieving $S_m = S_p$ requires that the friction coefficient c_{fm} in the model, and c_{fp} at prototype scale verify $c_{fm} = d\, c_{fp}$. This leads to large values of $k_{s,m}$ for values of d above 1 or 2, which could lead to undesired macro-rough flow conditions (too high $k_{s,\text{m}}/h_m$ values).

In all urban flood models so far, both the model material and the geometric distortion were kept unchanged for the whole range of considered flooding scenarios (Araud, 2012; Güney et al., 2014; Smith et al., 2016). Consequently, each model run corresponding to a given flooding scenario simulates actually a different value of the prototype-scale roughness height $k_{s,p}$. Indeed, if the flooding scenario is varied while predefined values of $k_{s,m}$ and d are kept unchanged, $S_m = S_p$ is obtained for different values of $k_{s,p}$ depending on the flooding scenario. Vice-versa, for a given value of the roughness height $k_{s,p}$ in the prototype, only a single value of d may lead to a correct similarity for friction (i.e., $S_m = S_p$) if the model material is kept unchanged. This value of d changes with the considered flooding scenario. The hydraulic modeller needs to be aware of this.

4.3.2 Recommendations

The current knowledge is not sufficient to identify in practice a clear-cut optimal value of the geometric distortion d for a particular prototype-scale flow scenario to be reproduced with a prescribed horizontal scale factor e_H. Nonetheless, some recommendations may be formulated.

First, an accessible range of d may be determined based on standard considerations on the minimum and maximum capacity of the available pumps as well as key instruments such as flowmeters. Next, as regards the accuracy of measurements, a minimum desirable value for d may be defined based on a sought accuracy for a given prototype-scale flow variable. For instance, prescribing a sought accuracy ε_p for the flow depths at prototype-scale leads to:

$$\varepsilon_m \, e_V = \varepsilon_m \frac{e_H}{d} \le \varepsilon_p \qquad \Rightarrow \qquad d \ge \frac{\varepsilon_m}{\varepsilon_p} e_H \tag{8}$$

where ε_m represents the scale-model measurements accuracy. For an objective of ε_p = 1 cm at prototype-scale and an experimental uncertainty ε_m = 1 mm in a model at scale 1:50 (e_H = 50), the minimum distortion would be d = 5. Similarly, aiming at a minimum value of the Reynolds number and/or of the flow depth in the scale model leads also to a lower bound for d.

Since our results show that there is a range of d in which the upscaled flow variables show a high sensitivity to the selected geometric distortion ($d < 5$ in the present case), it is of utmost importance that, as far as possible, two or three different distortion ratios are tested in the scale model. This procedure allows revealing the sensitivity of the upscaled flow variables to the selected range of values of d.

Finally, by comparing the friction numbers in the model and at prototype scale, it is possible to highlight to which extent friction effects are properly simulated or underestimated in the geometrically distorted scale model. The direction and magnitude of the resulting bias may be approached either based on the results presented here or with dedicated computational modelling (by simulating various values of d, as well as the prototype-scale flow). To some extent, such a procedure enables the modeller to offset the bias when interpreting the results of the scale model, or at least to be aware of the direction and approximate magnitude of this bias.

5 Conclusion

By systematically analysing the influence of changing the geometric distortion d in three laboratory scale models of urban flooding with intersecting streets (junction, bifurcation and simplified urban district), the following observations were made:

- in all configurations, the upscaled flow depths at the inlets exhibited a steep decrease (by up to 17 %) when the geometric distortion increased from $d = 1$ up to approximately $d = 5$, and they remained almost constant for d above 5;
- similarly, the flow discharge at the outlet of the branch that conveys the largest portion of the flow is greatly enhanced (by up to ~ 24 pp) for a geometric distortion varying up to $d = 5$, whereas above this threshold the discharge partition at the outlets remained almost constant;
- when the Froude number increases, the effect of distortion on the upscaled flow depths increases while the effect on discharge partition remains unchanged;
- a 2D computational model successfully reproduces the effect of geometric distortion on the upscaled flow depths and discharge partition at the street outlets, with maximum deviations (of the order of 4 %) between computations and observations occurring for large geometric distortions and high Froude numbers;
- the uncertainty in the upscaled flow variables is greatest for low geometric distortion ($d < 5$), and relatively low Froude number, due to the combined effect of measurement inaccuracies and uncertainties in setting the downstream boundary conditions.

These findings highlight that laboratory scale modelling remains challenging when a geometrically distorted scale model is deemed necessary, such as in the case of urban flooding. An important practical implication is that these novel experimental results indicate the direction and magnitude of the possible bias induced by geometric distortion for a broad range of flow cases (geometries and flooding scenarios), which is valuable for offsetting these effects in practical laboratory studies of urban flooding. The direction and magnitude of the resulting bias may also be approached based on dedicated computational modelling.

The present study shows some limitations as it is restricted to subcritical flows in simple urban layouts comprising only a few streets. Further research is needed to extend the knowledge on the effect of geometric distortion in more complex urban configurations, such as with steep bottom slopes leading to supercritical flow, unsteady conditions, or flow exchanges between the streets and the urban drainage system.

Acknowledgements

This research was funded by a fellowship from the "Fonds pour la formation à la Recherche dans l'Industrie et l'Agriculture" (FRIA, Belgium), as well as by a grant from "Fonds Spéciaux de la Recherche" (FSR) of the University of Liege. The support from the French National Research Agency (ANR) for the project DEUFI (ANR-18-CE01-0020) is also acknowledged. The authors gratefully acknowledge Prof. Nicolas Rivière for his insightful comments and suggestions. The data archiving is available on the repository Zenodo, from which they are freely accessible: https://doi.org/10.5281/zenodo.5113912.

Supplemental data

Supporting Information related to this article is available, including texts, figures and tables.

References

Araud, Q., 2012. Simulation des écoulements en milieu urbain lors d'un événement pluvieux extrême.

Arndt, R., Roberts, P., Wahl, T., 2000. Hydraulic Modeling: Concepts and Practice. American Society of Civil Engineers.

Arrault, A., Finaud-Guyot, P., Archambeau, P., Bruwier, M., Erpicum, S., Pirotton, M., Dewals, B., 2016. Hydrodynamics of long-duration urban floods: experiments and numerical modelling. Natural Hazards and Earth System Sciences 16, 1413–1429.

Assumpcao, T.H., Popescu, I., Jonoski, A., Solomatine, D.P., 2018. Citizen observations contributing to flood modelling: opportunities and challenges. Hydrology and Earth System Sciences 22, 1473–1489.

Brown, R., Chanson, H., 2013. Turbulence and Suspended Sediment Measurements in an Urban Environment during the Brisbane River Flood of January 2011. Journal of Hydraulic Engineering 139, 244–253.

Bruwier, M., Archambeau, P., Erpicum, S., Pirotton, M., Dewals, B., 2017. Shallow-water models with anisotropic porosity and merging for flood modelling on Cartesian grids. Journal of Hydrology 554, 693–709.

Castex, L., 1969. Quelques nouveautés sur les déversoirs pour la mesure des débits. La Houille Blanche N°5, 541–548.

Chanson, H., 1999. The hydraulics of open channel flow: An introduction, 1st ed., p. 512. ed. Edward Arnold, London, UK.

Chanson, H., Wang, H., 2013. Unsteady discharge calibration of a large V-notch weir. Flow Measurement and Instrumentation 29, 19–24.

Chen, Y., Zhou, H., Zhang, H., Du, G., Zhou, J., 2015. Urban flood risk warning under rapid urbanization. Environmental Research 139, 3–10.

Costabile, P., Costanzo, C., Lorenzo, G.D., Macchione, F., 2020. Is local flood hazard assessment in urban areas significantly influenced by the physical complexity of the hydrodynamic inundation model? Journal of Hydrology 580, 124231.

El Kadi Abderrezzak, K., Lewicki, L., Paquier, A., Rivière, N., Travin, G., 2011. Division of critical flow at three-branch open-channel intersection. Journal of Hydraulic Research 49, 231–238.

El Kadi Abderrezzak, K., Paquier, A., 2009. Numerical and Experimental Study of Dividing Open-Channel Flows. Journal of Hydraulic Engineering 135, 1111–1112.

Erpicum, S., Meile, T., Dewals, B. J., Pirotton, M., Schleiss, A.J., 2009. 2D numerical flow modeling in a macro-rough channel. International Journal for Numerical Methods in Fluids 61, 1227–1246.

Güney, M.S., Tayfur, G., Bombar, G., Elci, S., 2014. Distorted Physical Model to Study Sudden Partial Dam Break Flows in an Urban Area. Journal of Hydraulic Engineering 140, 05014006.

Heller, V., 2011. Scale effects in physical hydraulic engineering models. Journal of Hydraulic Research 49, 293–306.

Hettiarachchi, S., Wasko, C., Sharma, A., 2018. Increase in flood risk resulting from climate change in a developed urban watershed – the role of storm temporal patterns. Hydrology and Earth System Sciences 22, 2041–2056.

Jenkins, K., Surminski, S., Hall, J., Crick, F., 2017. Assessing surface water flood risk and management strategies under future climate change: Insights from an Agent-Based

Model. Science of The Total Environment 595, 159–168.

Jongman, Brenden, 2018. Effective adaption to rising flood risk. Nature communication 9.

Jonkman, S.N., 2005. Global Perspectives on Loss of Human Life Caused by Floods. Natural Hazards 34, 151–175.

Kitsikoudis, V., Becker, B.P.J., Huismans, Y., Archambeau, P., Erpicum, S., Pirotton, M., Dewals, B., 2020. Discrepancies in Flood Modelling Approaches in Transboundary River Systems: Legacy of the Past or Well-grounded Choices? Water Resources Management 34, 3465–3478.

Kobus, H., 1984. Symposium on Scale Effects in Modelling Hydraulic Structures. Water Resources Publications, Germany.

Leitao, J.P., Pena-Haro, S., Lüthi, B., Scheidegger, A., Vitry, M.M. de, 2018. Urban overland runoff velocity measurement with consumer-grade surveillance cameras and surface structure image velocimetry. Journal of Hydrology 565, 791–804.

Li, X., Erpicum, S., Bruwier, M., Mignot, E., Finaud-Guyot, P., Archambeau, P., Pirotton, M., Dewals, B., 2019. Technical note: Laboratory modelling of urban flooding: strengths and challenges of distorted scale models. Hydrology and Earth System Sciences 23, 1567–1580.

Li, X., Erpicum, S., Mignot, E., Archambeau, P., Rivière, N., Pirotton, M., Dewals, B., 2020. Numerical Insights Into the Effects of Model Geometric Distortion in Laboratory Experiments of Urban Flooding. Water Resources Research 56, e2019WR026774.

Liu, H., Wang, Y., Zhang, C., Chen, A.S., Fu, G., 2018. Assessing real options in urban surface water flood risk management under climate change. Natural Hazards 94, 1–18.

Macchione, F., Costabile, P., Costanzo, C., Lorenzo, G.D., 2019. Extracting quantitative data from non-conventional information for the hydraulic reconstruction of past urban flood events. A case study. Journal of Hydrology 576, 443–465.

McCabe, M.F., Rodell, M., Alsdorf, D.E., Miralles, D.G., Uijlenhoet, R., Wagner, W., Lucieer, A., Houborg, R., Verhoest, N.E.C., Franz, T.E., Shi, J., Gao, H., Wood, E.F., 2017. The future of Earth observation in hydrology. Hydrology and Earth System Sciences 21, 3879–3914.

Mignot, E., Li, X., Dewals, B., 2019. Experimental modelling of urban flooding: A review. Journal of Hydrology 568, 334–342.

Mignot, E., Paquier, A., Haider, S., 2006. Modeling floods in a dense urban area using 2D shallow water equations. Journal of Hydrology 327, 186–199.

Momplot, A., Kouyi, G.L., Mignot, E., Rivière, N., Bertrand-Krajewski, J.-L., 2017. Typology of the flow structures in dividing open channel flows. Journal of Hydraulic Research 55, 63–71.

Moy de Vitry, M., Kramer, S., Wegner, J.D., Leitao, J.P., 2019. Scalable flood level trend monitoring with surveillance cameras using a deep convolutional neural network. Hydrology and Earth System Sciences 23, 4621–4634.

Musolino, G., Ahmadian, R., Xia, J., Falconer, R.A., 2020. Mapping the danger to life in flash flood events adopting a mechanics based methodology and planning evacuation routes. Journal of Flood Risk Management n/a, e12627.

Neal, J.C., Bates, P.D., Fewtrell, T.J., Hunter, N.M., Wilson, M.D., Horritt, M.S., 2009. Distributed whole city water level measurements from the Carlisle 2005 urban flood event and comparison with hydraulic model simulations. Journal of Hydrology 368, 42–55.

Novak, P., Guinot, V., Jeffrey, A., Reeve, D.E., 2018. Hydraulic Modelling – an Introduction. CRC Press, London, UK.

Paquier, A., Bazin, P.-H., El Kadi Abderrezzak, K., 2020. Sensitivity of 2D hydrodynamic modelling of urban floods to the forcing inputs: lessons from two field cases. Urban Water Journal 17, 457–466.

Perks, M.T., Russell, A.J., Large, A.R.G., 2016. Technical Note: Advances in flash flood monitoring using unmanned aerial vehicles (UAVs). Hydrology and Earth System Sciences 20, 4005–4015.

Proudovsky, A.M., 1984. General Principles of Approximate Hydraulic Modelling, in: Kobus, H. (Ed.), Symposium Scale EffectsModellingHydraulicStructures. International Association for Hydraulic Reasearch (IAHR), pp. 0.2–1 – 0.2–14.

Riviere, N., Travin, G., Perkins, R.J., 2011. Subcritical open channel flows in four branch intersections. Water Resources Research 47, W10517.

Rubinato, M., Lashford, C., Goerke, M., 2020. Advances in experimental modelling of urban flooding. IWA - International Water Association, pp. 235–257.

Rubinato, M., Martins, R., Kesserwani, G., Leandro, J., Djordjevic, S., Shucksmith, J., 2017. Experimental calibration and validation of sewer/surface flow exchange equations in steady and unsteady flow conditions. Journal of Hydrology 552, 421–432.

Schindfessel, L., Creëlle, S., Mulder, T.D., 2015. Flow Patterns in an Open Channel Confluence with Increasingly Dominant Tributary Inflow. Water 7, 4724–4751.

Sharp, J.J., Khader, M.H.A., 1984. Scale effects in Harbour Models Invovling Permeable Rubble Mound Structures, in: Kobus, H. (Ed.), Symposium Scale EffectsModellingHydraulicStructures. International Association for Hydraulic Reasearch (IAHR), pp. 7.12–1 – 7.12–5.

Smith, G.P., Rahman, P.F., Wasko, C., 2016. A comprehensive urban floodplain dataset for model benchmarking. International Journal of River Basin Management 14, 345–356.

Teng, J., Jakeman, A.J., Vaze, J., Croke, B.F.W., Dutta, D., Kim, S., 2017. Flood inundation modelling: A review of methods, recent advances and uncertainty analysis. Environmental Modelling & Software 90, 201–216.

Wakhlu, O.N., 1984. Scale Effects in Hydraulic Model Studies, in: Kobus, H. (Ed.), Symposium Scale EffectsModellingHydraulicStructures. Technische Akademie Esslingen, pp. 2.13–1 – 2.13–6.

Wang, R.-Q., Mao, H., Wang, Y., Rae, C., Shaw, W., 2018. Hyper-resolution monitoring of urban flooding with social media and crowdsourcing data. Computers & Geosciences 111, 139–147.

Xia, J., Falconer, R.A., Wang, Y., Xiao, X., 2014. New criterion for the stability of a human body in floodwaters. Journal of Hydraulic Research 52, 93–104.

Yu, D., Lane, S.N., 2006. Urban fluvial flood modelling using a two-dimensional diffusion-wave treatment, part 1: mesh resolution effects. Hydrological Processes 20, 1541–1565.

Zhou, Q., Leng, G., Huang, M., 2018. Impacts of future climate change on urban flood volumes in Hohhot in northern China: benefits of climate change mitigation and adaptations. Hydrology and Earth System Sciences 22, 305–316.